

Multiscale Processes Leading to Heavy Precipitation in the Eastern Nepal Himalayas

HIDETAKA HIRATA^a, HATSUKI FUJINAMI,^b HIRONARI KANAMORI,^b YOTA SATO,^c MASAYA KATO,^b RIJAN B. KAYASTHA,^d MADAN L. SHRESTHA,^e AND KOJI FUJITA^c

^a Faculty of Data Science, Rissho University, Kumagaya, Japan

^b Institute for Space-Earth Environmental Research, Nagoya University, Nagoya, Japan

^c Graduate School of Environmental Studies, Nagoya University, Nagoya, Japan

^d Himalayan Cryosphere, Climate and Disaster Research Center, Department of Environmental Science and Engineering, School of Science, Kathmandu University, Dhulikhel, Nepal

^e Nepal Academy of Science and Technology, Kathmandu, Nepal

(Manuscript received 19 May 2022, in final form 12 January 2023)

ABSTRACT: The processes underlying heavy rainfall in the higher elevations of the Himalayas are still not well known despite their importance. Here, we examine the detailed process causing a heavy rainfall event, observed by our rain gauge network in the Rolwaling valley, eastern Nepal Himalayas, using ERA5 and a regional cloud-resolving numerical simulation. Heavy precipitation (112 mm day⁻¹) was observed on 8 July 2019 at Dongang (2790 m above sea level). Most of the precipitation (81 mm) occurred during 1900–2300 local time (LT). The synoptic-scale environment is characterized by a monsoon low pressure system (LPS) over northeastern India. The LPS lifted moisture upward from the lower troposphere and then horizontally transported it into the eastern Nepal Himalayas within the middle troposphere, increasing the content of the water vapor around Dongang. A mesoscale convective system passed over Dongang around the time of the intense precipitation. The numerical simulation showed that surface heat fluxes prevailed under the middle tropospheric (~500 hPa) southeasterly flow associated with the LPS around a mountain ridge on the upwind side of Dongang until 1900 LT, enhancing convective instability. Topographic lifting led to the release of the enhanced instability, which triggered the development of a mesoscale precipitation system. The southeasterly flow pushed the precipitation system northward, which then passed over Dongang during 2000–2200 LT, resulting in heavy precipitation. Thus, we conclude that the heavy precipitation came from the multiscale processes such as three-dimensional moisture transport driven by the LPS and the diurnal variation in heat fluxes from the land surface.


SIGNIFICANCE STATEMENT: Precipitation in the Himalayas is closely related to the hydrological cycle, floods, and landslide disasters in South Asia. Thus, elucidating the features of precipitation in the Himalayas is important. This study explored multiscale processes leading to a heavy precipitation event that was observed on 8 July 2019 at Dongang in the Rolwaling valley of the eastern Nepal Himalayas. We identified new processes producing heavy precipitation in the Himalayas: the three-dimensional synoptic-scale moisture transport driven by a monsoon low pressure system and the effect of the diurnal variation in heat fluxes from the land surface on the development and movement of a mesoscale precipitation system causing heavy precipitation. These findings broaden our understanding of heavy precipitation in the Himalayas.

KEYWORDS: Atmosphere-land interaction; Mesoscale systems; Monsoons; Precipitation; Cloud resolving models

1. Introduction

Precipitation in the Himalayas feeds the three major rivers, the Ganges, Indus, and Brahmaputra, of the Indian subcontinent (Immerzeel et al. 2010) and controls the behavior of Himalayan glaciers (Sakai et al. 2015; Sakai and Fujita 2017). In addition, precipitation around the Himalayas causes floods and landslides (Houze et al. 2011, 2017; Rasmussen and Houze 2012; Bohlinger et al. 2019). Thus, examining the features of precipitation in the Himalayas is valuable for an understanding of the mechanisms of the hydrological cycle and associated disasters in the South Asian monsoon region.

Some previous studies have examined the mechanism of heavy precipitation in Nepal (Bohlinger et al. 2017, 2019). Bohlinger et al. (2017) conducted a statistical investigation of synoptic atmospheric conditions and moisture sources related to heavy precipitation in Nepal using reanalysis and daily precipitation data obtained from meteorological stations of the Department of Hydrology and Meteorology in Nepal. They showed that middle tropospheric troughs and low pressure systems (LPSs) produced a synoptic atmospheric circulation that was favorable for heavy precipitation in Nepal. Moreover, they detected the presence of positive water vapor anomalies around Nepal on the day of heavy precipitation and suggested that the moisture that evaporated from the land around India, Pakistan, and Nepal significantly contributed to their formation. Bohlinger et al. (2019) examined the multiscale meteorological conditions of a heavy precipitation event in central Nepal that occurred in July 2007. They analyzed synoptic and mesoscale conditions using reanalysis data

 Denotes content that is immediately available upon publication as open access.

Corresponding author: Hidetaka Hirata, hirata@ris.ac.jp

DOI: 10.1175/JHM-D-22-0080.1

© 2023 American Meteorological Society. For information regarding reuse of this content and general copyright information, consult the AMS Copyright Policy (www.ametsoc.org/PUBSReuseLicenses).

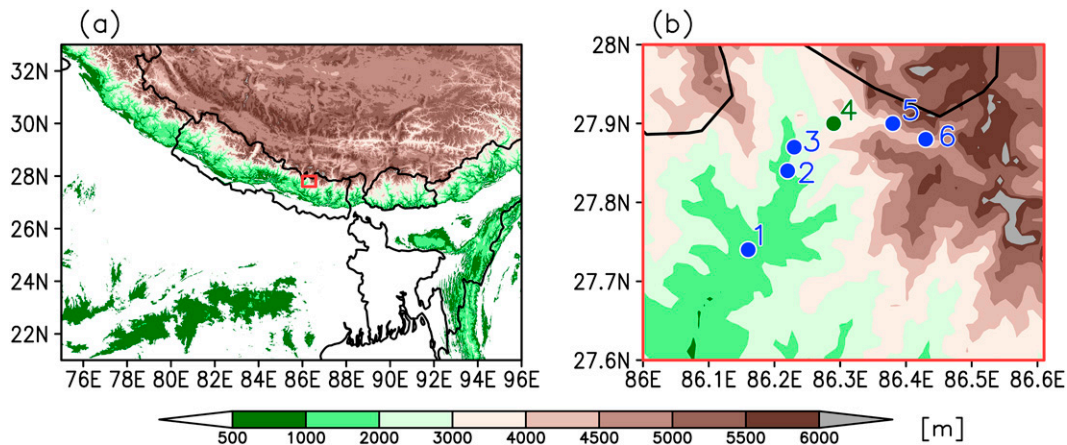


FIG. 1. (a) Topographic map based on NASA Shuttle Radar Topography Mission Global 30-arc-s elevation data (SRTMGL30; Rodriguez et al. 2006). (b) Topographic map around the Rolwaling valley in the eastern Nepal Himalayas shown within a red rectangle in (a). Closed circles indicate the locations of rain gauge stations (see details in Table 1). The numbers in this figure correspond to the station numbers listed in Table 1.

and a high-resolution numerical simulation, respectively. The numerical simulation showed that a system consisting of several convective cells caused this heavy precipitation event. Moreover, their results derived from reanalysis data indicated that the development of the mesoscale convective system was related to several synoptic-scale conditions, including moist air supply associated with a typical Indian monsoon break, moisture sources due to prior precipitation events, an upper-tropospheric trough, and an upslope flow. However, detailed analyses on the causes of heavy rainfall events in the higher elevations of the Himalayas are limited. The roles of monsoon LPSs in enhancing the mesoscale convection system over the slopes of the Himalayas are still poorly understood, although the statistical relationship between the LPSs and Himalayan precipitation is well known (e.g., Barros et al. 2004; Ueno et al. 2008; Bohlinger et al. 2017).

To better understand summer precipitation, including heavy rainfall events at higher elevations in the Himalayas and the mechanisms of its variability, we carried out an international collaborative research project (between Japan and Nepal) on precipitation in the Himalayas [Himalaya Precipitation Study (HiPRECS)]. We installed six rain gauges around the Rolwaling valley in May 2019 (Fig. 1 and Table 1; Fujinami et al. 2022a) to understand the detailed features of summer precipitation in the eastern Nepal Himalayas. Details of this observational project are presented in section 2a. Figure 2 shows the time series of daily precipitation observed at these six rain gauges between June and September 2019. For instance, at an altitude of 2790 m (shown by a green closed circle in Fig. 1b) at Dongang, daily precipitation of $112.4 \text{ mm day}^{-1}$ was observed on 8 July 2019. This daily precipitation value was the maximum across all measurements during the summer of 2019. Here, we focus on the heavy precipitation at Dongang and examine the mechanism behind this event.

The objective of this study was to explore the mechanism of the heavy precipitation observed at Dongang on 8 July 2019. As

with the heavy precipitation event highlighted by Bohlinger et al. (2019), multiscale meteorological processes might be responsible for the occurrence of the heavy precipitation at Dongang. Thus, we performed multiscale analyses of the heavy precipitation at Dongang. In section 3, we provide an overview of the basic features of precipitation at Dongang on 8 July 2019, using the observations obtained from our rain gauge network and infrared images from a geostationary satellite. In section 4, we investigate the synoptic-scale atmospheric environmental field of the heavy precipitation using reanalysis data. In section 5, we examine the mesoscale processes related to the generation of a precipitation system resulting in the heavy rainfall using a regional cloud-resolving simulation.

2. Data and numerical simulation

a. In situ observation

We installed rain gauges in Singati, Gongar, Simigaun, Dongang, Beding, and Na along the Rolwaling valley of the eastern Nepal Himalayas, leading to the Trambau/Trakading glaciers in mid-May 2019 under the HiPRECS project (Fig. 1) (Sunako et al. 2019; Fujinami et al. 2021, 2022a). The rain gauge stations were located at different altitudes, ranging from

TABLE 1. List of rain gauge stations installed by the international collaborative research teams (between Japan and Nepal) for recording precipitation in the Himalayas (HiPRECS: Himalaya Precipitation Study).

Station No.	Name	Latitude (°N)	Longitude (°E)	Altitude (m)
1	Singati	27.74	86.16	1001
2	Gongar	27.84	86.22	1311
3	Simigaun	27.87	86.23	2024
4	Dongang	27.90	86.29	2790
5	Beding	27.90	86.38	3761
6	Na	27.88	86.43	4183

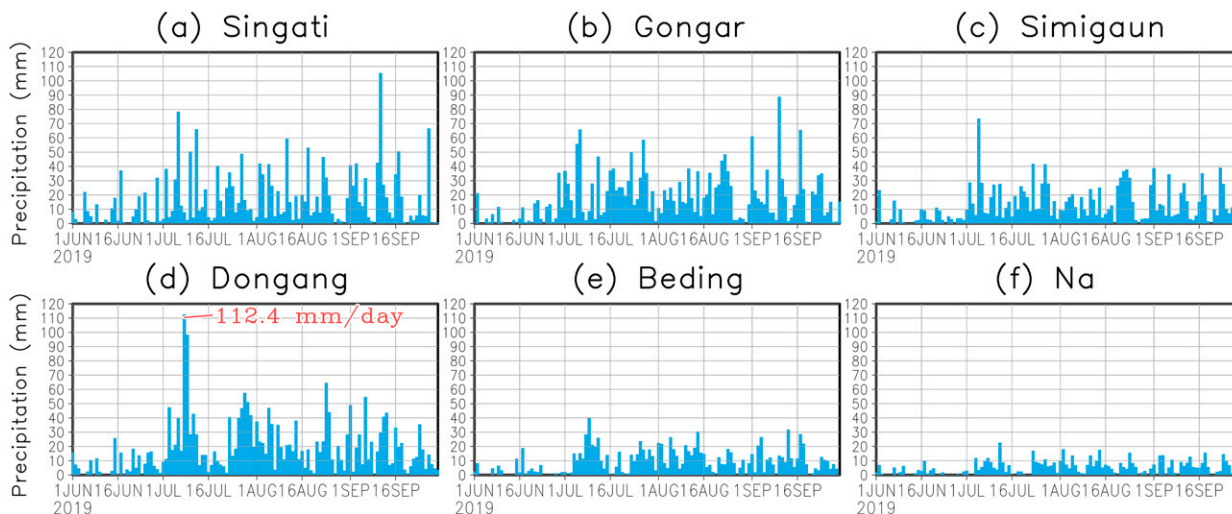


FIG. 2. Time series of daily precipitation observed at (a) Singati, (b) Gongar, (c) Simigaun, (d) Dongang, (e) Beding, and (f) Na from June to August 2019. Daily precipitation corresponds to the accumulated precipitation from 0001 to 2400 LT.

~1000 to ~4200 m above sea level (Table 1). All rain gauges were located in the valley bottom, except at Simigaun, which is positioned on the south-facing slope. Precipitation was measured using a tipping-bucket rain gauge with 0.2-mm resolution; this system has been previously used in the Himalayas by Ouyang et al. (2020). The total quantity of precipitation during the preceding hour was considered as the hourly precipitation. We used the unified local time (LT; UTC + 6 h) at 90°E instead of the Nepal standard time (UTC + 5 h 45 min). We successfully observed precipitation at all stations from mid-May to early October in 2019 without missing values. As the hourly air temperature was always greater than 0°C at all stations during June–September in this period (not shown), precipitation was in the form of rain.

b. Satellite data

We used infrared (channel 9: 10.8 μm) brightness temperature from the spinning enhanced visible and infrared imager of Meteosat Second Generation-1 (MSG1: *Meteosat-8*) Indian Ocean Data Coverage (IODC) in order to examine cloud activity related to precipitation events. Data were given on a 0.04° latitude \times 0.04° longitude grid with a 15-min interval.

We also utilized the Integrated Multi-satellitE Retrievals for GPM (IMERG) V06 B Level 3 final run precipitation product during 2000–20 (Huffman et al. 2019; Tan et al. 2019). The spatial and temporal resolution of this dataset is 0.1° latitude \times 0.1° longitude and 30 min, respectively. The variable used in this study is “precipitationCal.” IMERG was used for estimating the 99th percentile of daily precipitation (i.e., 24-h accumulation at LT; Fig. 3).

c. European Centre for Medium-Range Weather Forecasts fifth generation reanalysis (ERA5)

To examine the synoptic-scale atmospheric environmental field of the heavy precipitation event, we employed hourly data from the ERA5 dataset (Hersbach et al. 2020) provided

by the European Centre for Medium-Range Weather Forecasts. The horizontal resolution of the ERA5 data used in this study was 0.25° longitude \times 0.25° latitude. Daily mean ERA5 data (shown in Figs. 6 and 8) correspond to the time average of the hourly data from 0000 to 2300 LT on any day.

d. Cloud Resolving Storm Simulator

We used the Cloud Resolving Storm Simulator (CReSS; Tsuboki and Sakakibara 2002) to perform a numerical simulation of a precipitation system causing heavy precipitation. For cloud microphysics, we applied a bulk cold rain scheme, which predicts the mixing ratio of water vapor, cloud water, cloud ice, rain, snow, and graupel, and the concentrations of cloud ice, snow, and graupel (Murakami 1990; Ikawa and Saito 1991; Murakami et al. 1994). We employed a 1.5-order turbulent kinetic energy closure scheme (Deardorff 1980) for the parameterization of subgrid-scale turbulent eddies.

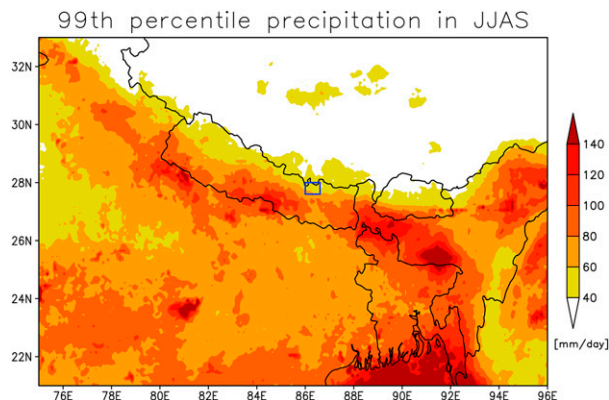


FIG. 3. The 99th percentile of daily precipitation during June–September, estimated using IMERG data during 2000–20.

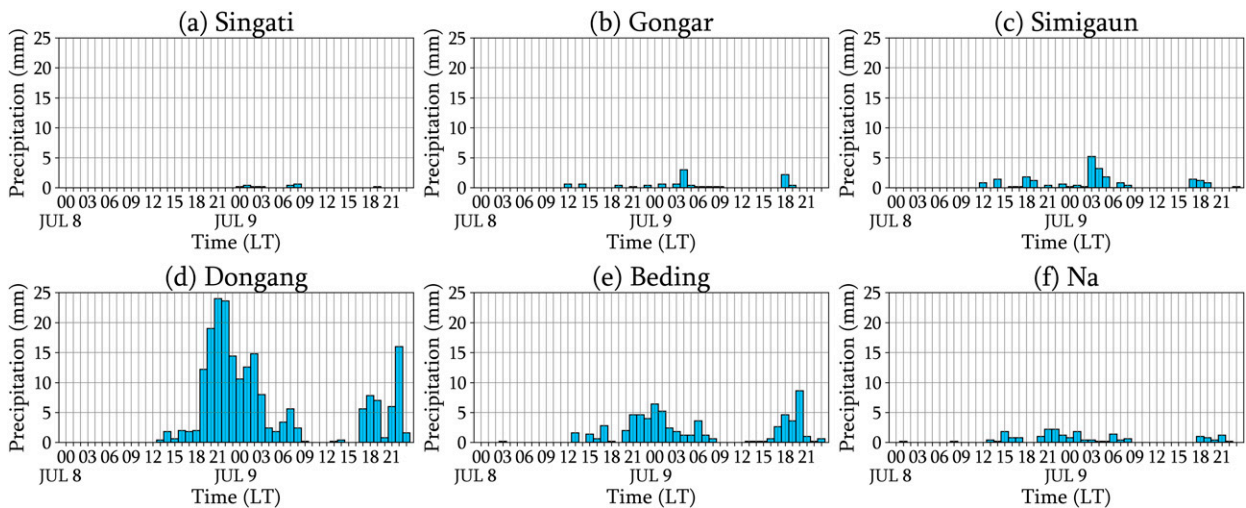


FIG. 4. Time series of hourly precipitation observed at (a) Singati, (b) Gongar, (c) Simigaun, (d) Dongang, (e) Beding, and (f) Na from 8 to 9 Jul 2019.

We used ERA5 hourly data as the initial and lateral boundary atmospheric conditions and the daily National Oceanic Atmospheric Administration (NOAA) optimal interpolation (OI) sea surface temperature (SST) with a spatial resolution of $0.25^\circ \times 0.25^\circ$ at the initial time of the simulation (Reynolds et al. 2007) as the SST conditions. We assumed that the SST field was fixed with time as the initial condition in the simulation. The terrain height in the simulation was based on National Aeronautics and Space Administration (NASA) Shuttle Radar Topography Mission Global 30-arc-s elevation data (SRTMGL30; Rodriguez et al. 2006).

The spacing of the horizontal grid was 0.02° for both longitude and latitude. We designated 45 vertical layers, with the lowest layer of 150 m and the height of the top level at 22 500 m. The model domain was $81.01^\circ\text{--}88.91^\circ\text{E}$, $26.51^\circ\text{--}29.37^\circ\text{N}$, including the Rolwaling valley (which is given in detail in Fig. 11). We set the initial and end times of the simulation at 1800 LT 7 July 2019 and 0000 LT 9 July 2019, respectively. The integral period included the day (8 July 2019) on which the heavy precipitation event was observed at Dongang.

3. Overview of the heavy precipitation event

First, to see how rare the precipitation event at Dongang on 8 July 2019 is, we estimated the 99th percentile of daily precipitation during June–September based on IMERG during 2000–20 (Fig. 3). The 99th percentile at a grid nearest Dongang was 54.5 mm day^{-1} . Moreover, the maximum 99th percentile around the rain gauge stations (domain of Fig. 1b corresponding to the blue rectangle in Fig. 3) was 66.8 mm day^{-1} . Thus, the precipitation event highlighted in this paper ($112.4 \text{ mm day}^{-1}$) can be regarded as an extreme event.

Next, to examine the diurnal cycle of the observed precipitation around the day of the heavy precipitation event, we plotted the time series of hourly precipitation observed at the six rain gauge stations from 8 to 9 July 2019 in Fig. 4. First, we checked the diurnal variation in precipitation at Dongang

(Fig. 4d). We did not observe any precipitation between 0000 and 1200 LT 8 July 2019; however, it started from 1200 LT 8 July 2019. We then noticed that the precipitation rapidly increased at approximately 1800 LT 8 July 2019. Between 2000 and 2200 LT 8 July 2019, we observed intense precipitation continuously exceeding 15 mm h^{-1} . More specifically, we found that the maximum value of hourly precipitation was recorded at 2100 LT (accumulated precipitation from 2001 to 2100 LT; 24.0 mm h^{-1}) 8 July 2019. Interestingly, the cumulative 4-h precipitation value between 1901 and 2300 LT was 81 mm, accounting for 72% of the daily precipitation on 8 July 2019. Thus, we concluded that most of the precipitation on 8 July 2019, occurred between 1900 and 2300 LT.

Next, we checked the time variation in the precipitation recorded at rain gauges other than that at Dongang. We noticed an increase in precipitation ($<5 \text{ mm h}^{-1}$) at Beding (Fig. 4e) and Na (Fig. 4f) between 1900 and 2300 LT 8 July 2019. Despite being weaker, the time variation in the precipitation at Beding and Na resembled that at Dongang. Since the linear distance from Dongang to Beding and Na is 8.85 and 13.95 km, we can speculate that a core of convective cells within a precipitation system just passed over Dongang and its stratiform portion passed over Beding and Na considering the structures of mesoscale convective systems (e.g., Parker and Johnson 2000). In contrast, the time variation in the precipitation at Singati (Fig. 4a), Gongar (Fig. 4b), or Simigaun (Fig. 4c) was not similar to that at Dongang.

To examine the features of a cloud system causing precipitation at Dongang, we analyzed the horizontal distribution of infrared brightness temperature from Meteosat from 1700 LT 8 July 2019 to 0000 LT 9 July 2019, as shown in Fig. 5. We found that just before the time of intense precipitation at Dongang (1800 LT 8 July 2019), a zonally elongated cloud system appeared on the southern side of Dongang (Fig. 5b). This cloud system was characterized by convective towers (brightness temperature $< 232 \text{ K}$). Moreover, we can see the

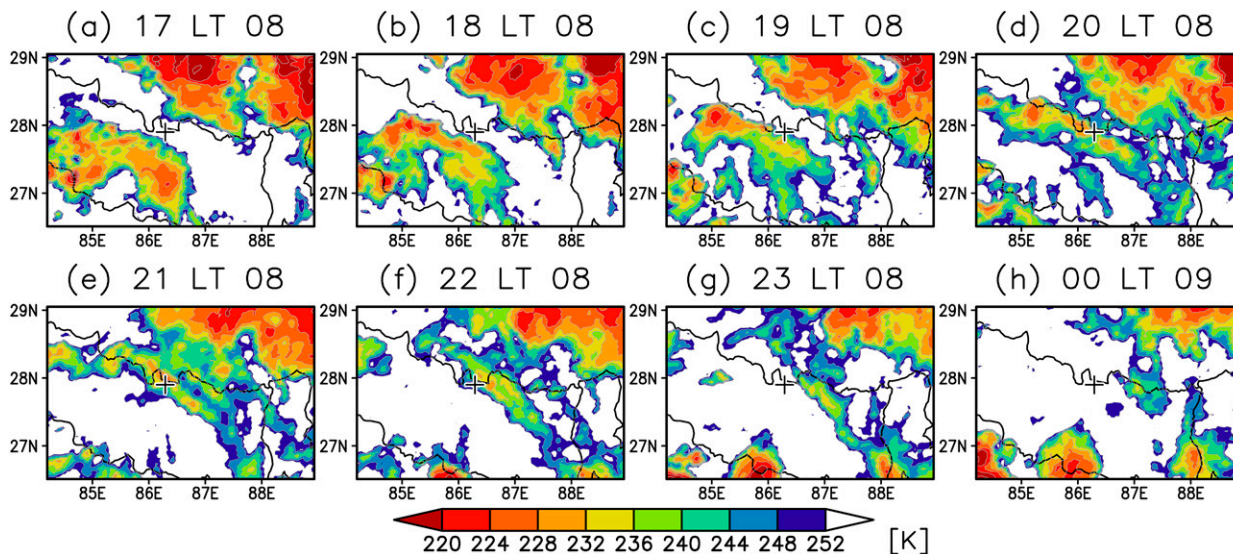


FIG. 5. (a)–(h) Maps of infrared brightness temperature derived from Meteosat from 1700 LT 8 Jul 2019 to 0000 LT 9 Jul 2019. The black cross indicates Dongang.

relatively high brightness temperature region (≥ 232 K), which corresponds to the stratiform portion of the system, around the convective towers. This system moved northward from 1900 LT 8 July 2019 (Figs. 5c–f). Interestingly, the convective towers passed over Dongang around the time (Figs. 5d,e) when the maximum hourly precipitation was observed at Dongang (2001–2100 LT). Thus, we believed that the convective towers brought the heavy precipitation at Dongang, and its stratiform portion resulted in the weaker precipitation at Beding and Na. The cloud system dissipated after 2300 LT (Figs. 5g,h). Precipitation exceeding 5 mm h^{-1} was observed at Dongang from after 2300 LT 8 July to 0300 LT 9 July (Fig. 4d), although significant cloud systems were not seen around Dongang in Fig. 5. Local enhancement of precipitation near Dongang or lower clouds along the valley may be related to the precipitation after 2300 LT.

Our analysis of the hourly precipitation data revealed that intense precipitation between 1900 and 2300 LT accounted for 72% of the daily precipitation on 8 July 2019 at Dongang (Fig. 4d). The horizontal distribution of the brightness temperature from Meteosat demonstrated that the convective towers within the zonally elongated cloud system passed over Dongang during the time of intense precipitation at Dongang (Figs. 5c–g). In section 5, we examine the features of this system using a cloud-resolving simulation.

4. Synoptic-scale environment of the heavy precipitation event

We investigated the synoptic-scale atmospheric environment of heavy precipitation at Dongang using ERA5. Figure 6 shows the horizontal distribution of total column water vapor (TCWV) anomalies as well as the geopotential height and horizontal wind at 500 hPa on 6, 8, 10, and 17 July 2019. We selected these days because 6 and 10 July are the days of the

genesis and dissipation of a monsoon LPS, 8 July is the day of the heavy precipitation, and 17 July is the driest day in July 2019 around the Rolwaling valley, as mentioned in detail later. We observed that a monsoon LPS was present to the southwest of the Rolwaling valley region (orange rectangle in Fig. 6b) on 8 July 2019, when heavy precipitation occurred at Dongang (Fig. 6b). The track of this LPS is also shown in Fig. 6. The track data were derived from the global track dataset of monsoon low pressure systems (Vishnu et al. 2020a,b). This LPS appeared over the eastern part of India at 0900 LT 8 July 2019 (Fig. 6a). Then, it migrated northwestward (Figs. 6a–c), finally dissipating at 1700 LT 10 July 2019 (Fig. 6c). Of note, the features of the genesis, dissipation, and migration of this LPS roughly corresponded to those of LPSs indicated in previous studies (Hatsuzuka et al. 2014; Hunt et al. 2016; Vishnu et al. 2020a).

We detected the presence of positive TCWV anomalies around the center of the LPS (Figs. 6a–c). This suggested that humid air was transported into the Rolwaling valley region by southeasterly winds over the northeastern quadrant of the LPS on 8 July 2019 (Fig. 6b). Indeed, the northwestward moisture fluxes were evident to the south of the Rolwaling valley region. The TCWV anomalies exceeded 2 kg m^{-2} around the Rolwaling valley on 8 and 10 July 2019 (Figs. 6b,c).

To assess the time variation in the content of water vapor around the Rolwaling valley, we explored the day-to-day variation in TCWV regionally averaged over the open orange box in Fig. 6 in July 2019, as illustrated in Fig. 7. We found that the regionally averaged TCWV was increased from ~ 24 to $\sim 26 \text{ kg m}^{-2}$ between 7 and 8 July. As shown in Fig. 6b, this increase in the quantity of water vapor appeared to be caused by the transport of LPS moisture. The maximum value of TCWV in July 2019 was recorded on 8 July. The relatively high TCWV values continued until 13 July, whereas they rapidly decreased after that date. Subsequently, the minimum

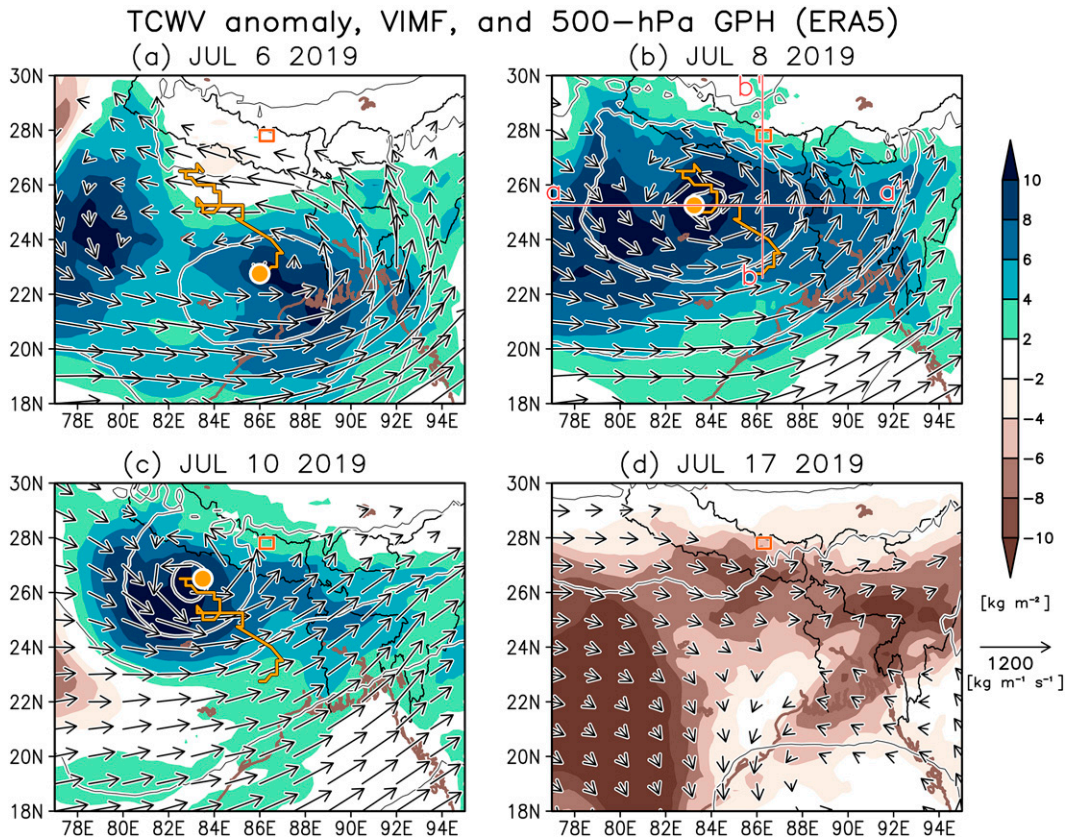


FIG. 6. (a)–(d) Maps of total column water vapor (TCWV) anomalies (shading; kg m^{-2}), vertically integrated moisture fluxes (arrows; $\text{kg m}^{-1} \text{s}^{-1}$), and 500-hPa geopotential height (contours; m) on 6, 8, 10, and 17 Jul 2019. The contour interval is 15 m. Moisture fluxes $\leq 100 \text{ kg m}^{-1} \text{s}^{-1}$ are not shown. Daily mean ERA5 data were used to create these panels. Anomalies are deviations from the monthly mean in July 2019. An orange rectangle and a yellow line indicate the Rolwaling valley region (area of Fig. 1b, which roughly corresponds to the location of our rain gauge stations) and the hourly track of a monsoon low pressure system (LPS), respectively. The yellow closed circle indicates the central location of the LPS at 0900 LT 6 Jul, 0600 LT 8 Jul, and 1700 LT 10 Jul in (a)–(c), respectively. Figure 8 was created along the red lines a–a' and b–b' in (b).

TCWV value in July 2019 was observed on 17 July. On 17 July, we did not observe any LPS around the South Asia region, while westerly winds associated with negative TCWV anomalies prevailed over the Rolwaling valley region, as shown in Fig. 6d. Our findings suggest that the increase in the content of water vapor in the valley was induced by the synoptic-scale circulation associated with the monsoon LPS.

To further examine the influence of the LPS on atmospheric conditions, we created vertical cross-sectional maps of meteorological elements along the lines a–a' and b–b' depicted in Fig. 6b (Fig. 8). Line a–a' zonally crosses the LPS center, whereas line b–b' meridionally crosses the Rolwaling valley region. We observed the presence of water vapor anomalies from the surface to 300 hPa around the LPS center (Fig. 8a). The raw water vapor value (black contour) was higher near the surface, while the maxima of these anomalies (shading) were found at approximately 500 hPa. In addition, we noticed a salient upward motion around these water vapor anomalies (Fig. 8a). It is thus conceivable that the upward motion, which was forced by frictional convergence near the

surface and convection organizing within the LPS system (Hunt et al. 2016; Fujinami et al. 2020; Diaz and Boos 2021), created water vapor anomalies in the middle troposphere by lifting the humid air near the surface. We found that the maxima of anomalies of equivalent potential temperature (θ_e) occurred at approximately 500 hPa around the LPS center (Fig. 8b). The θ_e value (black contour) was also higher around the positive θ_e anomalies (Fig. 8b) well matched those of water vapor anomalies (Fig. 8a), the increase in the water vapor quantity seemed to be responsible for the formation of these positive θ_e anomalies.

The features of water vapor and θ_e anomalies shown in the vertical cross-sectional maps along line a–a' (Figs. 8a,b) were also seen in the vertical cross-sectional maps along line b–b' (Figs. 8c,d). Moreover, Figs. 8c and 8d show that the southerly winds associated with the LPS were dominating around the positive water vapor and θ_e anomalies to the south of the observation stations in the middle troposphere (400–600 hPa). Of note, the light blue dashed line in Figs. 8c and 8d is drawn along the latitude of the rain gauge at Dongang. These results

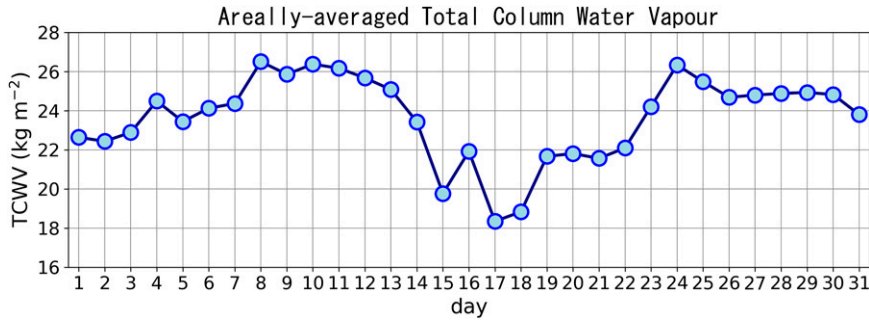


FIG. 7. Time series of daily TCWV averaged over the open orange box in Fig. 6 during July 2019.

suggested that the LPS circulation advected the air associated with the positive water vapor and θ_e anomalies into the Rolwaling valley region in the middle troposphere.

To verify the role of the LPS circulation in transporting air into the region around the rain gauge stations, we conducted a backward trajectory analysis using the ERA5 data. We

set the initial points of air parcels around the observation stations between 400 and 550 hPa. White dots in Figs. 8c and 8d correspond to the initial points. The initial time of the trajectory analysis was 2100 LT 8 July 2019, at the time of increased precipitation at Dongang (Fig. 4d). The modified Euler method was adopted as the time integration scheme, and

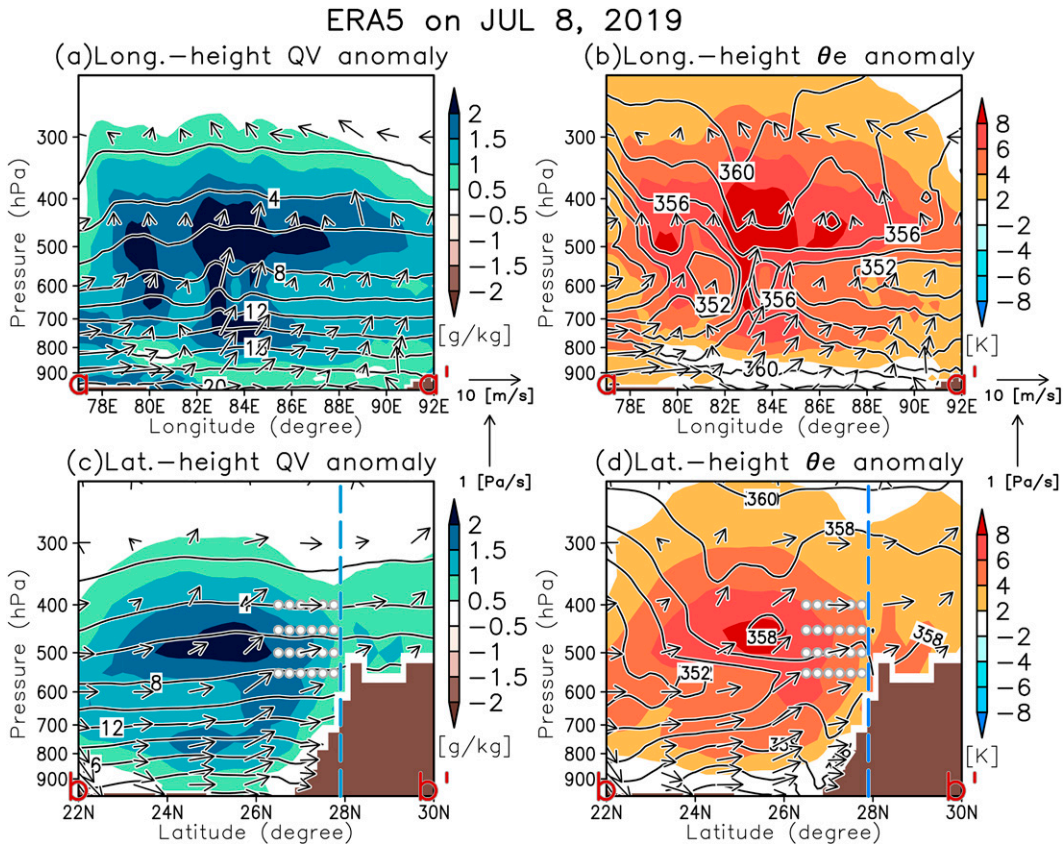


FIG. 8. (a) Longitude–height cross-sectional map of water vapor mixing ratio (contours; g kg^{-1}), its anomaly (shading; g kg^{-1}), and zonal and vertical winds (arrows) on 8 Jul 2019, along the red dashed line a–a' in Fig. 6b. Reference arrows for zonal and vertical winds are 10 m s^{-1} and 1 Pa s^{-1} , and the contour interval is 2 g kg^{-1} . Daily mean ERA5 data were used to create this map. Anomalies are deviations from the monthly mean in July 2019. (b) As in (a), but for equivalent potential temperature θ_e (contour; K) and its anomaly (shading; K). The contour interval is 2 K . (c),(d) As in (a) and (b), but for latitude–height cross-sectional map along the red dashed line b–b' in Fig. 6b, with meridional and vertical winds (arrows). The light blue dashed line illustrates the latitude of Dongang, and white closed circles indicate the initial locations of air parcels of a backward trajectory analysis.

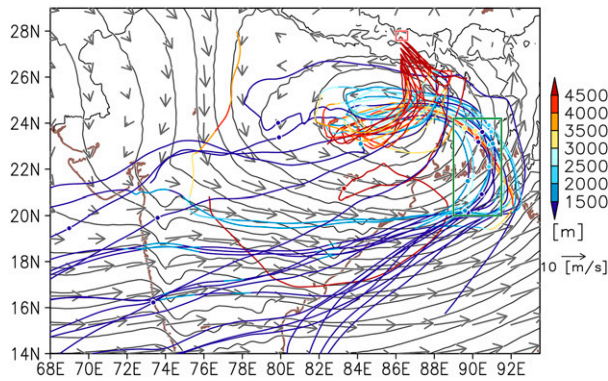


FIG. 9. Backward trajectories of air parcels calculated from 2100 LT 8 Jul 2019. Closed circles indicated the location of the parcels at 1700 LT 5 Jul 2019. The initial locations of parcels correspond to the closed white circles in Figs. 8c and 8d. The color of lines and circles denotes the heights (m) of air parcels. This map also shows geopotential height (contours; m) and horizontal wind vector (arrows; m s^{-1}) at 700 hPa of ERA5 averaged from 6 to 7 Jul 2019.

linear interpolation was used for the spatiotemporal interpolation of the data. The time integration of this analysis was executed in 1-min intervals.

Figure 9 illustrates the results of our backward trajectory analysis. We found that most air parcels moved from the Arabian Sea to the Bay of Bengal via large-scale monsoon circulation, and then northwestward from the head of the Bay of Bengal to the LPS, where they were trapped. Most parcels ascended from lower (<3000 m) to higher altitudes (>4500 m) around the center of the LPS. As shown in Fig. 8, the ascension of these parcels was caused by the upward motions in the vicinity of the LPS center. Finally, we noticed that the parcels migrated northward over the northeastern quadrant of the LPS, reaching the region around the observation stations.

Next, to understand the moisture transport relevant to the air parcels, we examined the time evolution of the water vapor content of typical parcels. We regarded parcels located within

the green open box ($89^{\circ}\text{--}91^{\circ}\text{E}$, $20^{\circ}\text{--}24^{\circ}\text{N}$) in Fig. 9 at 1700 LT 5 July 2019. Consequently, 16 parcels were extracted as typical parcels (24 parcels in total). Figures 10a and 10b show the ensemble-mean trajectory of the typical parcels and the time evolution of the ensemble mean of their moisture content. When the parcel migrated from the Arabian Sea to the Bay of Bengal, the moisture content was about 16 g kg^{-1} ; its variability was small (A–C in Fig. 10). As the parcel approached the continent, the moisture content decreased (C–D in Fig. 10). Moreover, while the parcel was incorporated into the LPS and then ascended, its moisture content further dropped (D–F in Fig. 10). This moisture decrease is seemingly due to condensation and the entrainment of the dryer air from the middle troposphere (Figs. 8a,c). Bohlinger et al. (2017, 2019) pointed out that moisture supply from the continent influenced heavy precipitation in Nepal. On the other hand, the parcels related to the heavy precipitation in question cannot receive moisture from the continent because most of the air parcels were located above a height of 1500 m (i.e., free atmosphere) during their passage over the continent (Figs. 9 and 10). These results suggest that the moisture transport from the Indian Ocean is pivotal to the heavy precipitation highlighted in this paper.

Our trajectory analysis also showed that the circulation of the LPS plays a vital role in the transport of moist and high θ_e air into the Rolwaling valley region. Thus, the LPS likely caused an increase in the quantity of water vapor around the Rolwaling valley on the day of heavy precipitation through the three-dimensional (3D) transport of moisture. In the next section, we examine the mechanism of occurrence of a mesoscale system that causes heavy precipitation in this synoptic-scale environment.

5. Mesoscale precipitation system causing the heavy precipitation event

Based on the results of the cloud-resolving numerical simulation introduced in section 2d, we examined the mesoscale features of a weather system related to heavy precipitation.

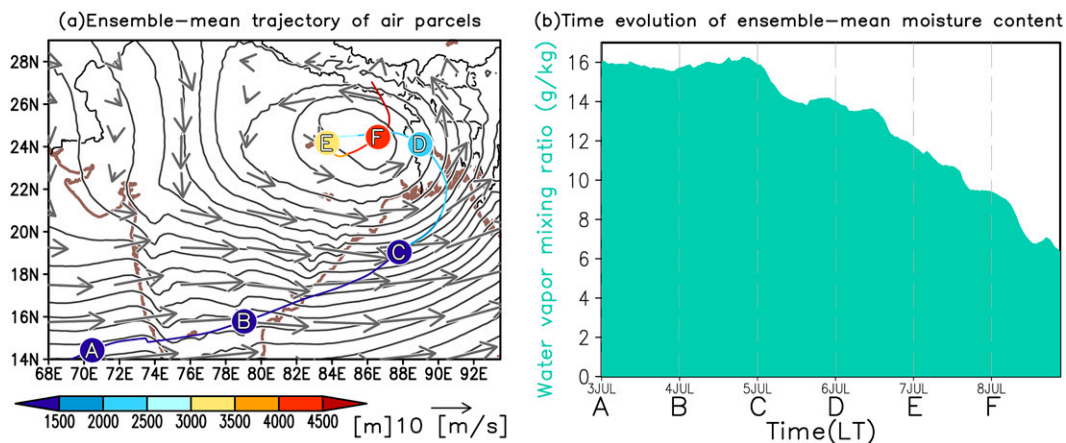


FIG. 10. (a) As in Fig. 9, but for the ensemble-mean trajectory of typical air parcels. (b) Time series of the ensemble mean of water vapor mixing ratio of typical air parcels. Symbols A–E in (b) correspond to the locations of the parcels depicted in (a).

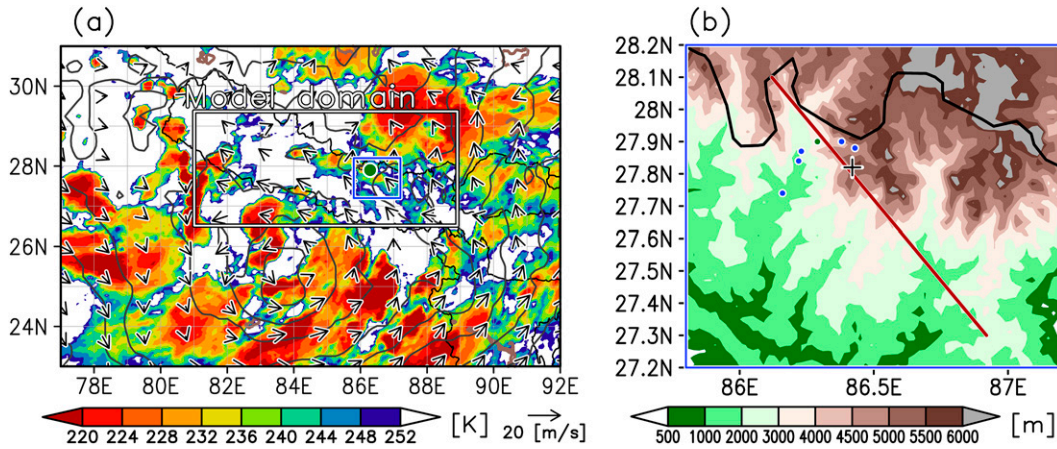


FIG. 11. (a) Map of infrared brightness temperature (shading; K) of Meteosat with geopotential height (contours; m) and horizontal wind vector (arrows; m s^{-1}) at 500 hPa of ERA5 at 2000 LT 8 Jul 2019. The model domain of the numerical simulation is shown in the white rectangle. Green closed circle indicates Dongang. (b) Topographic map of the region enclosed by the blue line in (a) in the numerical simulation. Closed circles indicate the locations of rain gauge stations.

Figure 11a shows the simulation domain (white rectangle) and the location of Dongang (green closed circle) along with meteorological conditions at 2000 LT 8 July 2019. The model domain covers the Rolwaling valley region and the region of the generation of the cloud system mentioned in section 3 (Fig. 5). Figure 11b shows the horizontal topographic distribution in the numerical simulation in the region enclosed by the blue line shown in Fig. 11a. The valley, in which rain gauges were installed, was roughly resolved.

Figure 12 shows the simulation of the horizontal distribution of surface precipitation and 400-hPa horizontal wind vectors from 1700 LT 8 July to 0000 LT 9 July 2019. Precipitation occurred around a mountain ridge (cross in Fig. 11b) on the

upwind side of Dongang (green closed circle in Fig. 12) at 1700 and 1800 LT (Figs. 12a,b). The zonally extending precipitation system developed around the south side of the observation stations at 1900 LT (Fig. 12c). Interestingly, we noticed that the zonally extending structure of the precipitation band seemed to be influenced by topography, because it formed along the slope of the mountains (Fig. 11b). The precipitation system migrated northward and then passed over Dongang at approximately 2000 LT 8 July. Subsequently, the system moved farther northward and dissipated (Figs. 12e–h).

Next, we compared the time series of hourly precipitation observed at our rain gauge stations on 8 July with the simulated hourly precipitation at the grids nearest these stations,

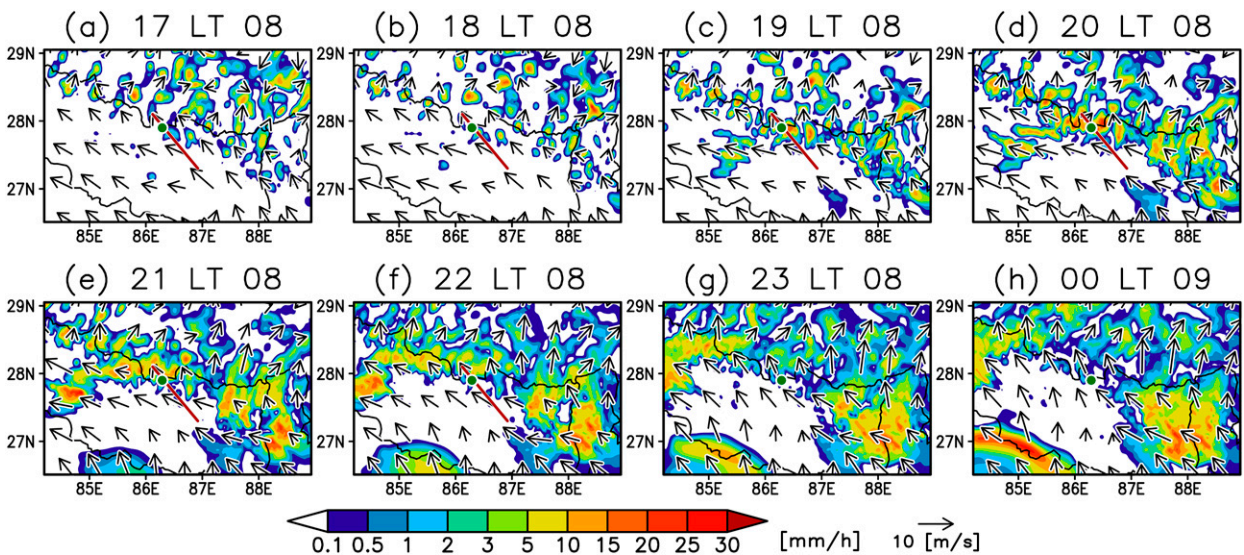


FIG. 12. (a)–(h) Maps of surface precipitation (shading; mm h^{-1}) and horizontal wind vectors at 400 hPa (arrows; m s^{-1}) in the numerical simulation from 1700 LT 8 Jul 2019 to 0000 LT 9 Jul 2019. The green closed circle indicates Dongang.

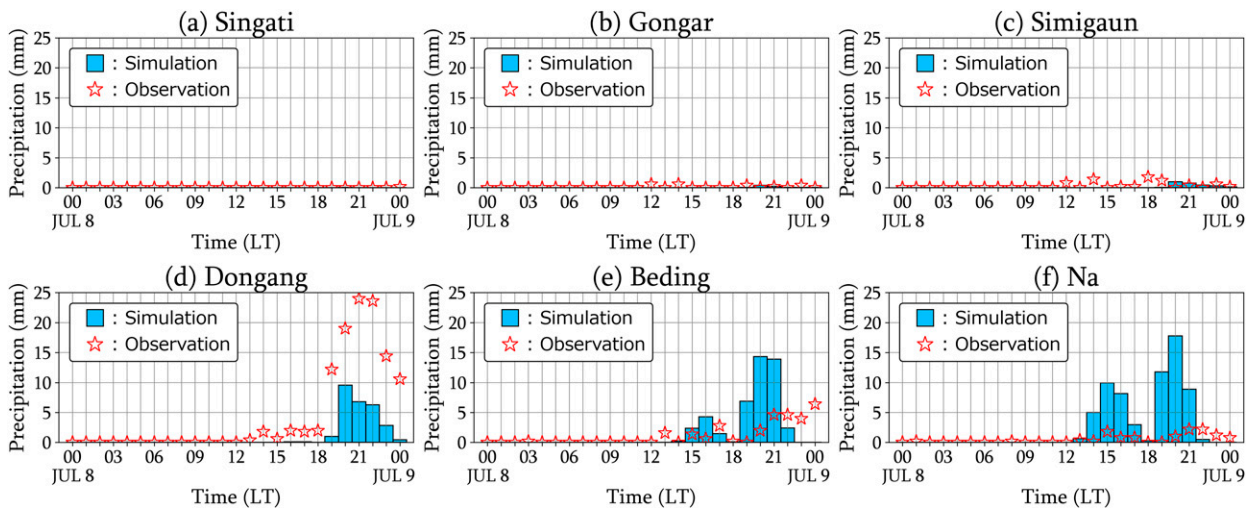


FIG. 13. Time series of hourly precipitation at (a) Singati, (b) Gongar, (c) Simigaun, (d) Dongang, (e) Beding, and (f) Na on 8 Jul 2019. Light blue bars and red open stars indicate the simulation and observation, respectively.

to validate the reproducibility of precipitation amount in the numerical model (Fig. 13). The simulation showed no rain on the day at Singati, Gongar, and Simigaun (Figs. 13a–c). Moreover, the model simulated the increase in the precipitation during 1900–2300 LT at Dongang, Beding, and Na (Figs. 13d–f). However, the simulation underestimated the precipitation at Dongang, while it overestimated the precipitation at Beding and Na. The cumulative 4-h precipitation value during 1900–2300 LT was 25.4 mm at Dongang in the simulation, which is merely 31% of the value observed (81 mm) in section 3. In the model, the maximum value of hourly precipitation (17.8 mm h^{-1}) was recorded at Na at 2000 LT (Fig. 13f). This value is 74% of the observed maximum (24 mm h^{-1}) at Dongang. Thus, the simulation roughly reproduced the intense hourly precipitation in the Rolwaling valley, although its location deviated from the observation of

about 10 km (since the linear distance between Dongang and Na is 13.95 km).

To consider the abovementioned difference in the precipitation amount at Dongang, Beding, and Na in the simulation, we indicate the horizontal distribution of hourly precipitation at the surface at 1900 and 2000 LT and topography around the Rolwaling valley (Fig. 14). Around 1900 and 2000 LT, precipitation was enhanced locally around the mountain ridge on the upstream side of Beding and Na ($\geq 15 \text{ mm h}^{-1}$). On the other hand, precipitation around Dongang was relatively weak ($< 10 \text{ mm h}^{-1}$). Consequently, the precipitation amount during 1900–2300 LT was lower at Dongang than at Beding and Na in the simulation. The surface precipitation occurred along mountain ridges all around the modeled area, suggesting that topography-induced ascent triggered the occurrence of precipitation. Thus, the structure of the topography and its

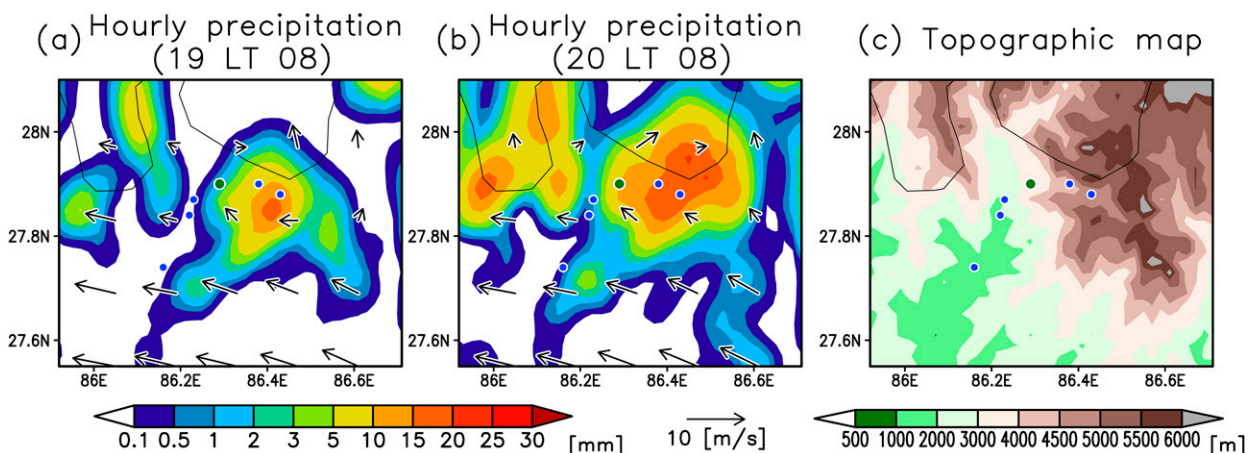


FIG. 14. Maps of hourly precipitation at the surface (shading; mm) and horizontal wind vectors at 400 hPa (arrows; m s^{-1}) in the numerical simulation at (a) 1900 LT and (b) 2000 LT 8 Jul 2019. (c) Topographic map in the numerical simulation. Closed circles indicate the locations of rain gauge stations.

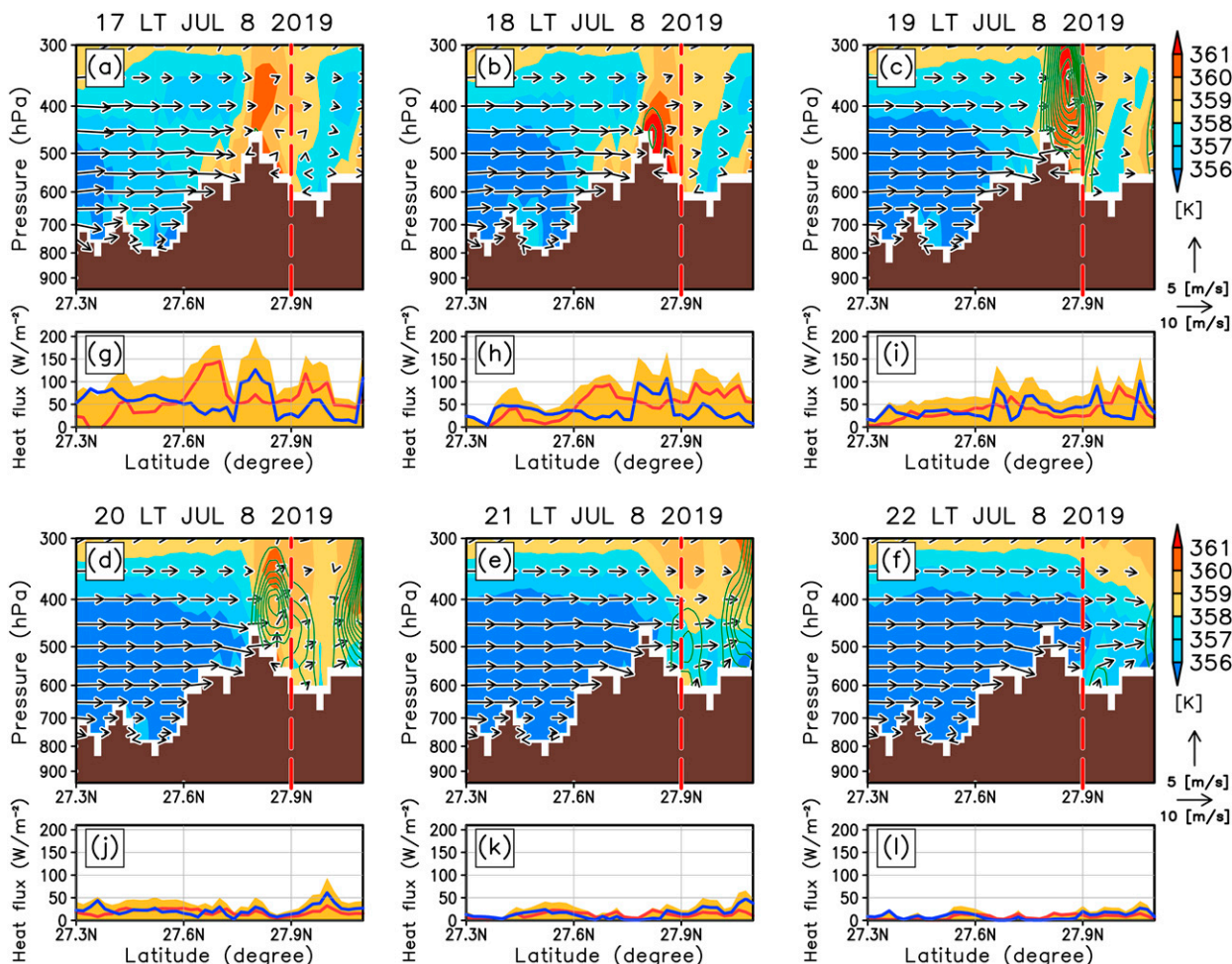


FIG. 15. (a)–(f) Vertical cross-sectional map of θ_e (shading; K), winds (arrows; m s^{-1}), and total mixing ratio of precipitating hydrometeors (contour; g kg^{-1}) along the red line illustrated in Figs. 11b and 12a–f from 1700 to 2200 LT 8 Jul 2019. The red dashed line illustrates the latitude of Dongang. Reference arrows for horizontal and vertical winds are 10 and 5 m s^{-1} . The contour interval is 0.3 g kg^{-1} , with the zero contour being suppressed. (g)–(l) Magnitude of surface sensible heat fluxes (red line), latent heat fluxes (blue line), and the sum of these fluxes (yellow shading) under the red line illustrated in Figs. 11b and 12a–f at each time.

impact on the atmosphere in the numerical simulation seems to influence the reproducibility of the precipitation in the simulation.

We found that the time at which the simulated precipitation system passed over Dongang roughly corresponded to that of intense precipitation at the rain gauge of Dongang (Figs. 4, 12, and 14). Moreover, the behavior of the simulated precipitation system resembled that of the observed cloud system passing over Dongang during the intense precipitation event (Figs. 5 and 12). Although it was underestimated, the precipitation increase during 1900–2300 LT was also simulated at Dongang in the simulation (Fig. 13). This underestimation may be due to the different locations of the intense precipitation area between the simulated and observed data (Fig. 14). These comparisons between the simulation and observations suggested that the numerical simulation successfully reproduced the features of the precipitation system causing heavy precipitation at Dongang. Therefore, we further explored the

processes that caused the development of the precipitation system.

To examine the features of the precipitation system, we analyzed the vertical cross section of θ_e (shading), winds (arrows), and total mixing ratio of precipitating hydrometeors (contour) along the red line illustrated in Figs. 11b and 12a–f from 1700 to 2200 LT 8 July 2019, as shown in Figs. 15a–f. The red dashed line in Figs. 15a–f illustrates the latitude of Dongang. Figures 15g–l illustrates the magnitude of the surface sensible and latent heat fluxes (red and blue lines) and their sum (yellow shading) along the red line in Figs. 11b and 12a–f. The location of a mountain ridge on the upwind side of the observation stations (Figs. 15a–f) is also confirmed in Fig. 11b. We observed that the southeasterly flow horizontally transported the air associated with a relatively low θ_e ($< 358 \text{ K}$) into the mountain ridge from the southern side within the middle troposphere (Figs. 15a–f), while the atmospheric boundary layer was modified by the heat fluxes from

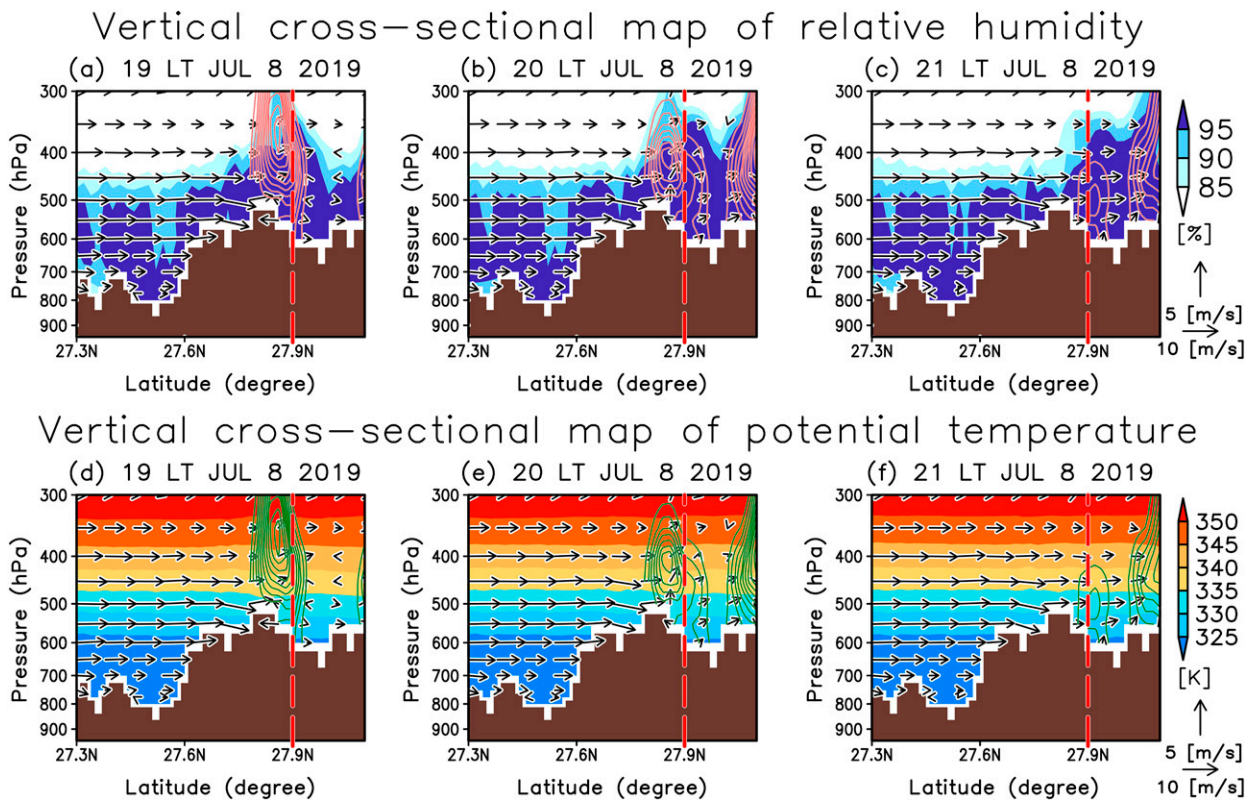


FIG. 16. (a)–(c) As in Figs. 15c–e, but for relative humidity (RH; shading; %). (d)–(f) As in Figs. 15c–e, but for potential temperature θ (shading; K).

the land surface around the mountain ridge from 1700 to 1900 LT (Figs. 15g–i). We further observed that the magnitudes of the sensible and latent heat fluxes were comparable ($\sim 150 \text{ W m}^{-2}$). As a result of the modification of the boundary layer, the convectively unstable conditions ($\partial\theta_e/\partial z < 0$) were enhanced near the surface at approximately 1800 LT (Fig. 15b). Accordingly, the enhanced instability was released, and the formation of precipitating hydrometeors was promoted in the vicinity of the mountain ridge around 1900 LT 8 July 2019 (Fig. 15c). The ascent forced by topography and thermal convection presumably brought about the release of instability. The timing of the precipitation intensification corresponded well with the time of increased surface precipitation (see Figs. 12c and 13). We then noticed that the total heat flux became $\sim 0 \text{ W m}^{-2}$ after 2000 LT (Figs. 15j–l). Moreover, we did not observe the formation of convectively unstable conditions and associated precipitation intensification after this rapid decrease in heat fluxes (Figs. 15e,f). Instead, we found that the precipitation system, which developed around the mountain ridge at 1900 LT (Fig. 15c), was pushed poleward by the convectively stable layer intruding from the south from 2000 LT (Figs. 15d–f). Consequently, the precipitation system migrated poleward and passed around Dongang between 2000 and 2100 LT (Figs. 15d,e).

To further explore the structure of the precipitation system, we also made the vertical cross-sectional map with respect to relative humidity (RH; Figs. 16a–c) and potential temperature θ (Figs. 16d–f) at 1900, 2000, and 2100 LT 8 July 2019.

Around the precipitation system, the RH exceeded 85% from the surface to the 300-hPa level (Figs. 16a–c). The atmospheric condition below the 400-hPa level was almost saturated ($\text{RH} \geq 95\%$), which seems to be related to the 3D synoptic moisture transport by the monsoon LPS as indicated in section 4. Mesoscale convective systems occurring in the central United States often attend gust fronts induced by latent cooling due to the evaporation of precipitation, and the fronts trigger the occurrence of new convective cells within the systems (e.g., section 9 in Markowski and Richardson 2010). However, such a saturated condition associated with the system in question is unfavorable for latent cooling due to the evaporation of precipitation hydrometeors. In fact, we cannot see the θ structure related to the cold pool and gust fronts under the system (Figs. 16d–f). These results also suggest that topographic lifting triggers the occurrence of the precipitation system as discussed above in Figs. 14 and 15.

To explore the cause of the drastic decrease in the surface heat fluxes after 1900 LT 8 July 2019, as shown in Figs. 15i and 15j, we examined the time series of land surface temperature (Fig. 17a), temperature in the bottom layer of the atmosphere in the simulation (Fig. 17a), and the differences between them (Fig. 17b) at a location around the mountain ridge on the upwind side of the rain gauge stations (cross in Fig. 11b). We observed that on 8 July 2019, the diurnal range of the temperature at the bottom layer of the atmosphere was $\sim 2 \text{ K}$ (blue dashed line in Fig. 17a), whereas that of the land

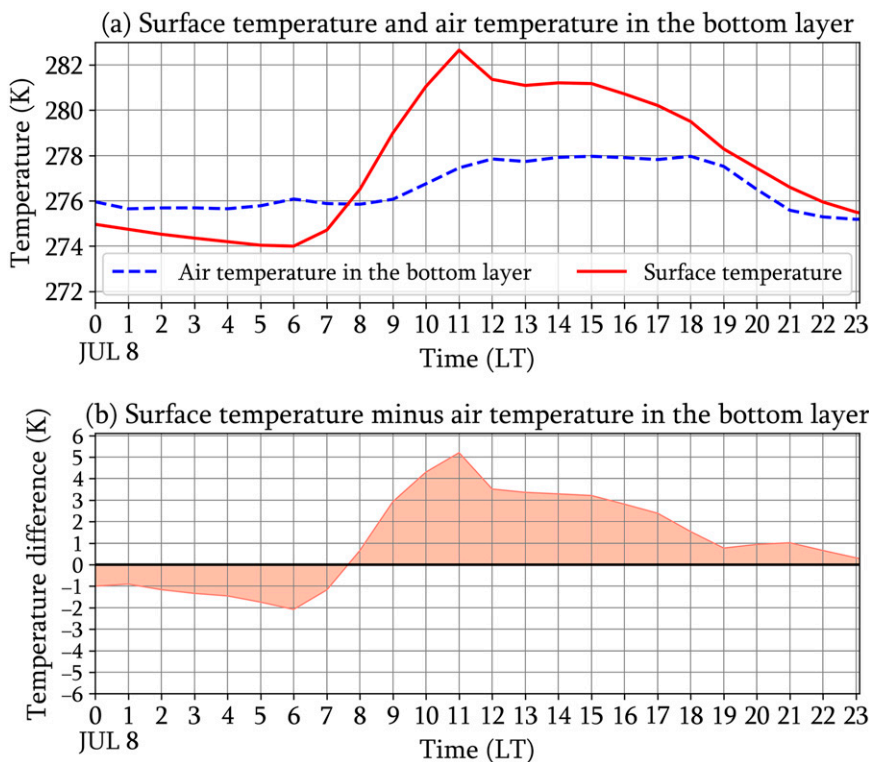


FIG. 17. (a) Time series of air temperature in the bottom layer of the model (red line) and land surface temperature (dashed blue line) in the numerical simulation at a location indicated by a cross in Fig. 11b on 8 Jul 2019. (b) Time series of the difference between the surface and air temperature in the bottom layer. The difference was calculated by subtracting the latter from the former.

surface temperature was ~ 9 K (red line in Fig. 17a). Thus, the diurnal range of the surface temperature was greater than that of the air temperature. The surface temperature reached its maximum at 1100 LT and decreased thereafter, dropping rapidly from 1800 LT onward owing to sunset. The difference between the surface and air temperature was also rapidly decreased after 1800 LT (Fig. 17b), which was attributed to the decrease in the surface temperature. After 1900 LT, the difference was < 1 K. These findings suggested that the rapid decline in the land surface temperature due to sunset reduced the difference between the surface and air temperature, eventually causing a rapid decrease in the surface heat fluxes after 1900 LT. Although we focused on the elements relevant to the surface sensible fluxes in Fig. 17, the diurnal variation in the surface latent heat fluxes was also mainly caused by the diurnal variation in the surface temperature (not shown).

6. Discussion

a. Synoptic-scale atmospheric environmental field of heavy precipitation

Here, we discuss the synoptic-scale atmospheric environmental field of heavy precipitation at Dongang on 8 July 2019, based on the results shown in section 4. The monsoon LPS was situated around northeastern India to the southwest of Dongang on the day of the heavy precipitation event (Fig. 6b).

The results obtained from ERA5 indicated that LPS played a dual role in the formation of the environmental field suitable for the occurrence of heavy precipitation.

The first role was to moisten the troposphere. More specifically, the ascent associated with the LPS transported the near-surface moisture vertically (Figs. 8–10). Consequently, positive anomalies in the water vapor were evident from the surface to the upper troposphere around the LPS (Figs. 8a,c). Moreover, the increase in the quantity of water vapor led to an increase in θ_e (Figs. 8b,c). Therefore, the positive water vapor anomalies and θ_e were especially high in the middle troposphere at approximately 500 hPa (Fig. 8).

The second role was to transport moist air into the region around the rain gauge stations. The LPS created cyclonic circulation in the middle troposphere over northeastern India on the day of heavy precipitation (Figs. 6b, 8, and 9). As the atmospheric conditions in the middle troposphere around the LPS were characterized by increased moisture, the cyclonic circulation of the LPS horizontally imported moist air into the region around the observation stations in the middle troposphere (Figs. 8–10). These successive LPS-induced processes increased the moisture content around the observation stations (Fig. 7), creating an environmental field favorable for the occurrence of heavy precipitation.

Bohlinger et al. (2017) pointed out that LPSs and middle tropospheric troughs were related to synoptic-scale conditions

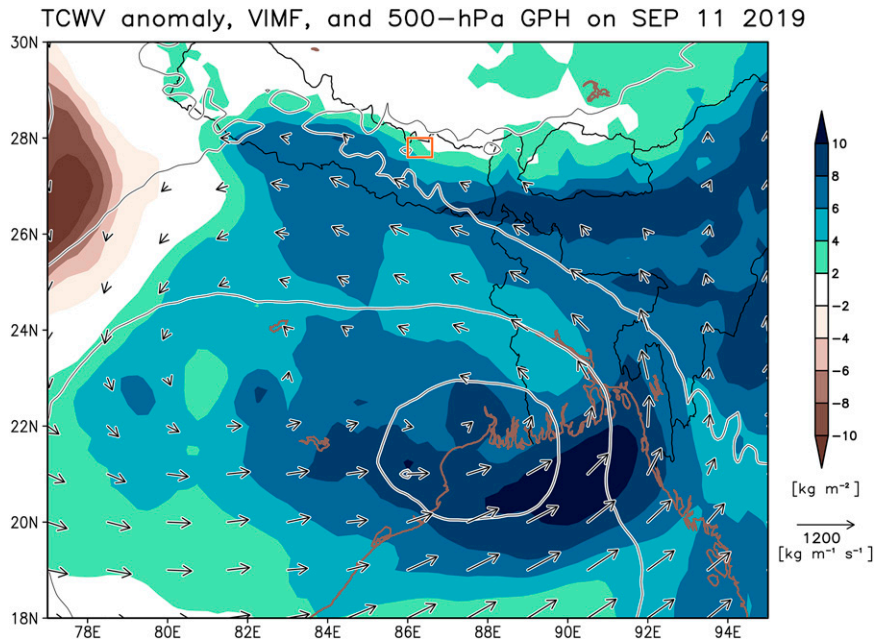


FIG. 18. As in Fig. 6, but for 11 Sep 2019. Anomalies are deviations from the monthly mean in September 2019.

leading to heavy precipitation events in the Nepal Himalayas. [Bohlinger et al. \(2019\)](#) suggested that a Rossby wave train in midlatitudes sustained a middle tropospheric trough around Nepal. Consistent with [Bohlinger et al. \(2017\)](#), our results showed that LPS was involved in the synoptic-scale conditions of heavy precipitation at Dongang on 8 July 2019. However, we did not detect the influence of a middle tropospheric trough in our study (Fig. 6). Additionally, a Rossby wave train was not found around Nepal on 8 July 2019 (data not shown). Moreover, [Bohlinger et al. \(2017, 2019\)](#) indicated that the zonal wind component was westerly around the Nepal Himalayas in the middle troposphere, which is related to the break condition of the Indian summer monsoon (e.g., [Joseph and Sijikumar 2004](#)), when heavy precipitation occurred. In contrast, the zonal wind component was easterly around the Nepal Himalayas on the day of heavy precipitation (Fig. 6b). The synoptic condition of our event (Figs. 6 and 9) was characterized by the flow pattern of the active condition of the Indian summer monsoon (e.g., [Joseph and Sijikumar 2004](#)). The comparisons between our study and previous studies show the diversity of synoptic-scale atmospheric environmental fields of heavy precipitation in the Nepal Himalayas. Thus, to further deepen our understanding of synoptic-scale conditions related to heavy precipitation in the Himalayas, we should perform pattern classification of synoptic-scale conditions and examine the features of each pattern.

Our results suggested that heavy precipitation in the Himalayas was related to the 3D moisture transport associated with LPSs. [Dong et al. \(2016\)](#) also pointed out that 3D moisture transport influenced summer rainfall variability over the southwestern Tibetan Plateau. [Dong et al. \(2016\)](#) indicated that convective systems lifted moist air from the surface

over central-eastern India, which was then advected into the southwestern Tibetan Plateau by middle-tropospheric circulation (see Fig. 7 in [Dong et al. 2016](#)). They emphasized that such processes contributed to an increase in precipitation over the southwestern Tibetan Plateau. Moreover, they suggested that monsoon LPSs were involved in the organization and development of convective systems over central-eastern India. Although the focus areas differ between [Dong et al. \(2016\)](#) and our study, our results (Figs. 8–10) were similar to the mechanism of 3D moisture transport in the high-altitude region discussed by them. Moreover, previous studies ([Lang and Barros 2002](#); [Barros et al. 2004](#); [Ueno et al. 2008](#); [Sugimoto et al. 2021](#)) reported that precipitation in the Himalayas was increased when monsoon LPSs were situated to the south of the Himalayas. Increases in precipitation examined in the aforementioned studies might have also been related to the LPS-driven 3D moisture transport proposed in our study. These similarities between this and previous studies suggested that the LPS-driven 3D moisture transport has a vital role in the occurrence of heavy precipitation and increase in precipitation in the high-altitude region over South Asia, including the Himalayas and the Tibetan Plateau.

Our rain gauge network captured heavy precipitation exceeding 100 mm day^{-1} not only at Dongang but also at Singati (1001 m above sea level), which is the lowest-altitude station of the six stations (Fig. 1b and Table 1), during June–September 2019 (Fig. 2). Daily precipitation of $105.4 \text{ mm day}^{-1}$ was observed at Singati on 11 September 2019 (Fig. 2). It may be meaningful to compare the synoptic features of the heavy precipitation at Dongang with those at Singati. Thus, we, here, briefly introduce the synoptic environment of the heavy precipitation at Singati (Fig. 18). The TCWV anomalies exceeded

2 kg m^{-2} around the Rolwaling valley on the day of the heavy precipitation at Singati. The magnitude of the TCWV anomaly is comparable with that of the heavy precipitation that occurred at Dongang (Fig. 6b). Moreover, a monsoon LPS was located around the head of the Bay of Bengal on 11 September. Although the center of the LPS is located far from the rain gauge stations as compared with that on 8 July, the circulation associated with this LPS seems to contribute to the increase in the moisture around the rain gauge stations on 11 September. Moisture fluxes to the south of the Rolwaling valley were weak on 11 September, as compared with those on July 8 (Fig. 6b). This is due to the long distance between the valley and the LPS center. Such synoptic conditions on 11 September may favor the occurrence of a mesoscale system producing heavy precipitation at Singati. We will examine the mesoscale system related to the heavy precipitation at Singati in detail in a separate paper, as such analyses are beyond the scope of this study.

b. Mesoscale precipitation system causing heavy precipitation

Here, we discuss the mesoscale precipitation system producing heavy precipitation at Dongang based on the results derived from the cloud-resolving numerical simulation shown in section 5. Heavy precipitation occurred in an environment where the moist southeasterly winds blew against the eastern Nepal Himalayas in the middle troposphere, as discussed in section 6a. Atmospheric conditions were convectively stable on the upwind side of the eastern Nepal Himalayas within the middle troposphere (Fig. 15). However, the bottom of the convectively stable layer received heat and moisture from the land surface around the mountain ridge on the upwind side of Dongang (Figs. 15a–c). Consequently, convectively unstable conditions were formed and enhanced over the mountain ridge until 1800 LT 8 July 2019 (Fig. 15b). Owing to the release of enhanced convective instability, the mesoscale precipitation system rapidly developed after 1900 LT 8 July 2019 (Figs. 15c,d). The topography-induced ascent seems to trigger the release of the instability (Figs. 14–16). The land surface temperature was drastically decreased after 1800 LT 8 July 2019, owing to sunset (Fig. 17), suppressing heat fluxes from the land surface to the atmosphere (Figs. 15g–i). Because of the weakening of heat fluxes, the enhanced convective instability was not observed around the eastern Nepal Himalayas (Figs. 15c–f). As a result, the southeasterly winds associated with the convectively stable layer pushed the mesoscale precipitation system poleward, which then passed over Dongang around 2000–2200 LT 8 July 2019 (Figs. 15d–f). The timing of the passage of the system over Dongang roughly corresponded to the timing of the increase in precipitation observed at Dongang during 1900–2300 LT 8 July 2019 (Figs. 4d and 13d). Thus, we concluded that the mesoscale precipitation system caused the heavy precipitation at Dongang.

We highlight that the diurnal variation in surface heat fluxes over the Himalayas is a key factor driving the development and migration of mesoscale precipitation systems. Although some previous studies reported that mesoscale precipitation

systems brought precipitation in the Himalayas (Romatschke and Houze 2011; Rasmussen and Houze 2012) and Nepal (Bohlinger et al. 2019), they did not consider the influence of diurnal variation of surface heat fluxes over the Himalayas on these systems. Our study suggested that the role of surface heat fluxes is important for a better understanding of the mechanism behind the occurrence of mesoscale precipitation systems in the Himalayas.

Similar to Dongang, a less intense increase in precipitation during 1900–2300 LT 8 July 2019, was also observed at Beding and Na (Figs. 4e,f). However, such an increase in precipitation was not observed at Singati, Gongar, and Simigaun (Figs. 4a–c). The observed features of the precipitation were well simulated by our simulation (Fig. 13). Considering the mechanism of the precipitation system and the width of the valley might help us understand the regional differences in precipitation variations. The width of the valley floor in which Dongang, Beding, and Na are situated is narrow. Thus, a precipitation system developing over the mountain ridges on the upwind side will reach these stations before it dissipates as shown in Fig. 14. On the other hand, the width of the valley is wider around Singati, Gongar, and Simigaun. Because the distance from Singati, Gongar, and Simigaun to the mountain ridges on the upwind side is greater, a precipitation system growing around the mountain ridges will likely dissipate before reaching these points. Although precipitation exceeding 5 mm h^{-1} was simulated around the mountain ridge on the upstream side of Singati at 1900 LT July 2019 (Fig. 14a), the precipitation at Singati was very weak ($<0.5 \text{ mm h}^{-1}$; Fig. 13a). Thus, we believe that the width of the valley is the key factor leading to the regional differences in precipitation variations.

As shown in Fig. 4, heavy precipitation was mainly observed at night, consistent with the nighttime peak of the diurnal precipitation cycle in the Nepal Himalayas (Fujinami et al. 2021). The climatological mean diurnal precipitation cycle around the higher-elevation stations such as Dongang, Beding, and Na showed two peaks: one is at 1500–1700 LT, and the other is at 2300–0200 LT (Fujinami et al. 2021). The upslope flow due to the heated slope surface is responsible for the precipitation peak in the afternoon, while the nocturnal acceleration of low-level monsoon flow from the Gangetic Plain causes large-scale moisture convergence around the slopes leading to the nocturnal precipitation peak (Fujinami et al. 2021, 2022b). On 8 July, precipitation was suppressed in the afternoon, whereas precipitation reached its maximum earlier than the climatological nocturnal precipitation peak at Dongang (Fig. 4). Stronger synoptic-scale wind conditions by the LPS might suppress thermally driven slope winds in the daytime more than usual, enhancing the large-scale nocturnal monsoon southerlies from the lower to middle troposphere resulting in an earlier and larger maximum of precipitation at Dongang. The mechanism by which the interaction between the diurnal cycle and LPS promotes heavy precipitation events remains an important issue for future research.

The behavior of the simulated precipitation system effectively explains the time variation in the precipitation observed at Dongang. However, this cannot explain the particularly intense precipitation occurring at Dongang relative to Beding

and Na. Our simulation also cannot reproduce the stronger precipitation at Dongang than at Beding and Na (Figs. 13 and 14). There are two possible explanations for this. First, it might be difficult to reproduce the behavior of individual convective cells within a precipitation system in a numerical simulation. Second, a more local effect, which cannot be resolved in our simulation with a horizontal resolution of 0.02° , might have caused the local enhancement of precipitation at Dongang. Further understanding the precipitation features around the Rolwaling valley region, which is characterized by complicated geography, will require more high-resolution numerical simulations and highly dense observations. We plan to address this issue through a new Asian regional hydroclimatological project, termed the Asian Precipitation Experiment (AsiaPEX; Terao et al. 2023).

7. Summary

We conducted in situ observations of surface precipitation along the Rolwaling valley in the eastern Nepal Himalayas in the summer of 2019 under an international collaborative research project between Japan and Nepal, HiPRECS. Our research captured a heavy precipitation event ($112.4 \text{ mm day}^{-1}$) at Dongang at an elevation of 2790 m (Figs. 1 and 2). This event can be regarded as an extreme event (Fig. 3). Here, we attempted to reveal some aspects of this heavy precipitation event and explore the multiscale processes leading to this event by utilizing observations, reanalysis data, and a regional cloud-resolving numerical simulation. The main findings of this study are summarized as follows.

- Especially intense precipitation (81 mm) was observed at Dongang during 1900–2300 LT 8 July 2019 (Fig. 4). Infrared imagery showed that a south-originating zonally elongating cloud system passed over Dongang at the time of intense precipitation (Fig. 5).
- Results obtained from ERA5 revealed that a monsoon LPS existed around the northeastern part of India on the day of heavy precipitation (Fig. 6b), playing a dual role in forming the synoptic-scale environment favorable for heavy precipitation. The first role was to humidify the atmosphere through the vertical transport of moisture from the surface to the upper troposphere (Figs. 8–10). In particular, positive water vapor anomalies were evident within the middle troposphere at $\sim 500 \text{ hPa}$ (Fig. 8). The second role was the horizontal transport of moisture into the region around Dongang within the middle troposphere by the cyclonic circulation of the LPS (Figs. 8–10). Owing to these effects, the quantity of water vapor was increased around the Rolwaling valley on the day of heavy precipitation (Figs. 6 and 7).
- A cloud-resolving numerical simulation with a horizontal resolution of 0.02° demonstrated that the diurnal variation of surface heat fluxes drove the development and migration of a mesoscale precipitation system, resulting in heavy precipitation. Sensible and latent heat fluxes from the land surface were enhanced under the southeasterly flow around the mountain ridge on the upwind side of the Rolwaling valley until 1900 LT 8 July 2019, in turn enhancing

convective instability around the mountain ridge (Fig. 15). Topographic lifting caused the release of the instability (Figs. 14 and 15). This release led to the development of a mesoscale convective system around 1900 LT 8 July 2019 (Fig. 15c). After 1800 LT 8 July 2019, heat fluxes were suppressed by the decline in the land surface temperature due to sunset (Figs. 15 and 17). The heat flux became $\sim 0 \text{ W m}^{-2}$ after 2000 LT 8 July 2019. Consequently, the southeasterly winds associated with the convectively stable layer pushed the mesoscale precipitation system poleward (Figs. 15d–f), passing over the Rolwaling valley and causing intense precipitation at Dongang around 2000–2200 LT 8 July 2019 (Figs. 12–15).

The findings of this study established the involvement of multiscale meteorological processes in heavy precipitation events in the Himalayas, which is in agreement with Bohlinger et al. (2019). Moreover, we found new processes relevant to heavy precipitation in the Himalayas: the 3D synoptic-scale moisture transport induced by the monsoon LPS and the effect of the diurnal variation in heat fluxes from the land surface on the intensification and migration of the mesoscale precipitation system. We aim to examine whether such multiscale processes are involved in other heavy precipitation events. Although extratropical influence on our case was not found as discussed in section 6a, it may play an important role in other heavy precipitation cases (e.g., Vellore et al. 2016; Bohlinger et al. 2017, 2019). Further investigation on the role of extratropical influence is required to comprehend processes underlying heavy precipitation events in the Himalayas. As the activities of monsoon LPSs are influenced by low-frequency phenomena, such as tropical intraseasonal oscillations (Fujinami et al. 2014; Hatsuzuka et al. 2014; Hatsuzuka and Fujinami 2017) and El Niño–Southern Oscillation (Vishnu et al. 2020a), these phenomena might modulate precipitation variability in the Himalayas by varying LPS activities. We will discuss this issue in a separate study.

Acknowledgments. The authors thank the three anonymous reviewers and the Editor, Craig R. Ferguson, for their very helpful comments. This study was supported by JSPS KAKENHI (Grants JP18KK0098, JP21H01164, JP20H02252, and JP19H01375) and the Collaborative Research Project on Computer Science with High-Performance Computing at Nagoya University. This study was JSPS and SNSF under the Joint Research Projects (JRPs; Grant 20191503). Computation of the numerical simulation was carried out using the supercomputer “Flow” at the Information Technology Center, Nagoya University. This work was partly conducted as a joint research program with the Center for Environmental Remote Sensing (CEReS), Chiba University (2022).

Data availability statement. In situ precipitation data for Rolwaling valley in 2019 summer are available from PANGAEA (<https://doi.pangaea.de/10.1594/PANGAEA.943230>). ERA5 reanalysis data (<https://doi.org/10.5065/D6X34W69>) were downloaded from the Copernicus climate-change service (C3S) climate data store (<https://cds.climate.copernicus.eu>). NOAA

provided the OISST (<https://www.ncei.noaa.gov/products/optimum-interpolation-sst>). SRTM30 was provided by NASA EOSDIS Land Processes DAAC (<https://doi.org/10.5067/MEaSURES/SRTM/SRTMGL30.002>). We used infrared brightness temperature data from MSG1 (Meteosat 8)-IODC. CEReS archived and provided the data (<https://ceres.chiba-u.jp/en/top-eng/>). IMERG dataset can be downloaded from NASA's Earth Science Data Systems (https://disc.gsfc.nasa.gov/datasets/GPM_3IMERGHH_06/summary). We used the global track dataset of monsoon low pressure systems, which were downloaded from the Zenodo repository (<https://doi.org/10.5281/zenodo.3890646>), to show the track of the monsoon LPS in Fig. 6. The CReSS model was developed by the Institute for Space–Earth Environmental Research (ISEE), Nagoya University (<https://www.isee.nagoya-u.ac.jp/en/co-re.html>).

REFERENCES

- Barros, A. P., G. Kim, E. William, and S. W. Nesbitt, 2004: Probing orographic controls in the Himalayas during the monsoon using satellite imagery. *Nat. Hazards Earth Syst. Sci.*, **4**, 29–51, <https://doi.org/10.5194/nhess-4-29-2004>.
- Bohlinger, P., A. Sorteberg, and H. Sodemann, 2017: Synoptic conditions and moisture sources actuating extreme precipitation in Nepal. *J. Geophys. Res. Atmos.*, **122**, 12653–12671, <https://doi.org/10.1002/2017JD027543>.
- , —, C. Liu, R. Rasmussen, H. Sodemann, and F. Ogawa, 2019: Multiscale characteristics of an extreme precipitation event over Nepal. *Quart. J. Roy. Meteor. Soc.*, **145**, 179–196, <https://doi.org/10.1002/qj.3418>.
- Deardorff, J. W., 1980: Stratocumulus-capped mixed layers derived from a three-dimensional model. *Bound.-Layer Meteor.*, **18**, 495–527, <https://doi.org/10.1007/BF00119502>.
- Diaz, M., and W. R. Boos, 2021: The influence of surface heat fluxes on the growth of idealized monsoon depressions. *J. Atmos. Sci.*, **78**, 2013–2027, <https://doi.org/10.1175/JAS-D-20-0359.1>.
- Dong, W., and Coauthors, 2016: Summer rainfall over the southwestern Tibetan Plateau controlled by deep convection over the Indian subcontinent. *Nat. Commun.*, **7**, 10925, <https://doi.org/10.1038/ncomms10925>.
- Fujinami, H., T. Yasunari, and A. Morimoto, 2014: Dynamics of distinct intraseasonal oscillation in summer monsoon rainfall over the Meghalaya–Bangladesh–western Myanmar region: Covariability between the tropics and mid-latitudes. *Climatic Dyn.*, **43**, 2147–2166, <https://doi.org/10.1007/s00382-013-2040-1>.
- , H. Hirata, M. Kato, and K. Tsuboki, 2020: Mesoscale precipitation systems and their role in the rapid development of a monsoon depression over the Bay of Bengal. *Quart. J. Roy. Meteor. Soc.*, **146**, 267–283, <https://doi.org/10.1002/qj.3672>.
- , K. Fujita, N. Takahashi, T. Sato, H. Kanamori, S. Sunao, and R. B. Kayastha, 2021: Twice-daily monsoon precipitation maxima in the Himalayas driven by land surface effects. *J. Geophys. Res. Atmos.*, **126**, e2020JD034255, <https://doi.org/10.1029/2020JD034255>.
- , —, Y. Sato, H. Kanamori, R. Kayastha, and R. B. Kayastha, 2022a: Precipitation observations in Rolwaling valley, eastern Nepal Himalayas, in summer 2019. PANGAEA, accessed 14 April 2022, <https://doi.pangaea.de/10.1594/PANGAEA.943230>.
- , T. Sato, H. Kanamori, and M. Kato, 2022b: Nocturnal southerly moist surge parallel to the coastline over the western Bay of Bengal. *Geophys. Res. Lett.*, **49**, e2022GL100174, <https://doi.org/10.1029/2022GL100174>.
- Hatsuzuka, D., and H. Fujinami, 2017: Effects of the South Asian monsoon intraseasonal modes on genesis of low pressure systems over Bangladesh. *J. Climate*, **30**, 2481–2499, <https://doi.org/10.1175/JCLI-D-16-0360.1>.
- , T. Yasunari, and H. Fujinami, 2014: Characteristics of low pressure systems associated with intraseasonal oscillation of rainfall over Bangladesh during boreal summer. *Mon. Wea. Rev.*, **142**, 4758–4774, <https://doi.org/10.1175/MWR-D-13-00307.1>.
- Hersbach, H., and Coauthors, 2020: The ERA5 global reanalysis. *Quart. J. Roy. Meteor. Soc.*, **146**, 1999–2049, <https://doi.org/10.1002/qj.3803>.
- Houze, R. A., Jr., K. L. Rasmussen, S. Medina, S. R. Brodzik, and U. Romatschke, 2011: Anomalous atmospheric events leading to the summer 2010 floods in Pakistan. *Bull. Amer. Meteor. Soc.*, **92**, 291–298, <https://doi.org/10.1175/2010BAMS3173.1>.
- , L. A. McMurdie, K. L. Rasmussen, A. Kumar, and M. M. Chaplin, 2017: Multiscale aspects of the storm producing the June 2013 flooding in Uttarakhand, India. *Mon. Wea. Rev.*, **145**, 4447–4466, <https://doi.org/10.1175/MWR-D-17-0004.1>.
- Huffman, G. J., E. F. Stocker, D. T. Bolvin, E. J. Nelkin, and J. Tan, 2019: GPM IMERG final precipitation L3 half hourly 0.1 degree × 0.1 degree V06. Goddard Earth Sciences Data and Information Services Center (GES DISC), accessed 19 October 2022, https://disc.gsfc.nasa.gov/datasets/GPM_3IMERGHH_06/summary.
- Hunt, K. M. R., A. G. Turner, P. M. Inness, D. E. Parker, and R. C. Levine, 2016: On the structure and dynamics of Indian monsoon depressions. *Mon. Wea. Rev.*, **144**, 3391–3416, <https://doi.org/10.1175/MWR-D-15-0138.1>.
- Ikawa, M., and K. Saito, 1991: Description of a nonhydrostatic model developed at the Forecast Research Department of the MRI. MRI Tech. Rep. 28, 238 pp., https://www.mri-jma.go.jp/Publish/Technical/DATA/VOL_28/28.pdf.
- Immerzeel, W. W., L. P. H. van Beek, and M. F. P. Bierkens, 2010: Climate change will affect the Asian water towers. *Science*, **328**, 1382–1385, <https://doi.org/10.1126/science.1183188>.
- Joseph, P. V., and S. Sijikumar, 2004: Intraseasonal variability of the low-level jet stream of the Asian summer monsoon. *J. Climate*, **17**, 1449–1458, [https://doi.org/10.1175/1520-0442\(2004\)017<1449:IVOTLJ>2.0.CO;2](https://doi.org/10.1175/1520-0442(2004)017<1449:IVOTLJ>2.0.CO;2).
- Lang, T. J., and A. P. Barros, 2002: An investigation of the onsets of the 1999 and 2000 monsoons in central Nepal. *Mon. Wea. Rev.*, **130**, 1299–1316, [https://doi.org/10.1175/1520-0493\(2002\)130<1299:AIOTOO>2.0.CO;2](https://doi.org/10.1175/1520-0493(2002)130<1299:AIOTOO>2.0.CO;2).
- Markowski, P., and Y. Richardson, 2010: *Mesoscale Meteorology in Midlatitudes*. Wiley-Blackwell, 407 pp.
- Murakami, M., 1990: Numerical modeling of dynamical and microphysical evolution of an isolated convective cloud—The 19 July 1981 CCOPE cloud. *J. Meteor. Soc. Japan*, **68**, 107–128, https://doi.org/10.2151/jmsj1965.68.2_107.
- , T. L. Clark, and W. D. Hall, 1994: Numerical simulations of convective snow clouds over the Sea of Japan: Two-dimensional simulation of mixed layer development and convective snow cloud formation. *J. Meteor. Soc. Japan*, **72**, 43–62, https://doi.org/10.2151/jmsj1965.72.1_43.
- Ouyang, L., K. Yang, H. Lu, Y. Chen, Lazhu, X. Zhou, and Y. Wang, 2020: Ground-based observations reveal unique valley precipitation patterns in the central Himalaya. *J. Geophys. Res. Atmos.*, **125**, e2019JD031502, <https://doi.org/10.1029/2019JD031502>.

- Parker, M. D., and R. H. Johnson, 2000: Organizational modes of midlatitude mesoscale convective systems. *Mon. Wea. Rev.*, **128**, 3413–3436, [https://doi.org/10.1175/1520-0493\(2001\)129<3413:OMOMMC>2.0.CO;2](https://doi.org/10.1175/1520-0493(2001)129<3413:OMOMMC>2.0.CO;2).
- Rasmussen, K. L., and R. A. Houze, Jr., 2012: A flash-flooding storm at the steep edge of high terrain disaster in the Himalayas. *Bull. Amer. Meteor. Soc.*, **93**, 1713–1724, <https://doi.org/10.1175/BAMS-D-11-00236.1>.
- Reynolds, R. W., T. M. Smith, C. Liu, D. B. Chelton, K. S. Casey, and M. G. Schlax, 2007: Daily high-resolution-blended analyses for sea surface temperature. *J. Climate*, **20**, 5473–5496, <https://doi.org/10.1175/2007JCLI1824.1>.
- Rodriguez, E., C. S. Morris, and J. E. Belz, 2006: A global assessment of the SRTM performance. *Photogramm. Eng. Remote Sens.*, **72**, 249–260, <https://doi.org/10.14358/PERS.72.3.249>.
- Romatschke, U., and R. A. Houze Jr., 2011: Characteristics of precipitating convective systems in the South Asian monsoon. *J. Hydrometeor.*, **12**, 3–26, <https://doi.org/10.1175/2010JHM1289.1>.
- Sakai, A., and K. Fujita, 2017: Contrasting glacier responses to recent climate change in high-mountain Asia. *Sci. Rep.*, **7**, 13717, <https://doi.org/10.1038/s41598-017-14256-5>.
- , T. Nuimura, K. Fujita, S. Takenaka, H. Nagai, and D. Lamsal, 2015: Climate regime of Asian glaciers revealed by GAMDAM glacier inventory. *Cryosphere*, **9**, 865–880, <https://doi.org/10.5194/tc-9-865-2015>.
- Sugimoto, S., K. Ueno, H. Fujinami, T. Nasuno, T. Sato, and H. G. Takahashi, 2021: Cloud-resolving-model simulations of nocturnal precipitation over the Himalayan slopes and foothills. *J. Hydrometeor.*, **22**, 3171–3188, <https://doi.org/10.1175/JHM-D-21-0103.1>.
- Sunako, S., K. Fujita, A. Sakai, and R. B. Kayastha, 2019: Mass balance of Trambau glacier, Rolwaling region, Nepal Himalaya: In-situ observations, long-term reconstruction and mass-balance sensitivity. *J. Glaciol.*, **65**, 605–616, <https://doi.org/10.1017/jog.2019.37>.
- Tan, J., G. J. Huffman, D. T. Bolvin, and E. J. Nelkin, 2019: Diurnal cycle of IMERG V06 precipitation. *Geophys. Res. Lett.*, **46**, 13 584–13 592, <https://doi.org/10.1029/2019GL085395>.
- Terao, T., and Coauthors, 2023: AsiaPEX: Challenges and prospects in Asian precipitation research. *Bull. Amer. Meteor. Soc.*, <https://doi.org/10.1175/BAMS-D-20-0220.1>, in press.
- Tsuboki, K., and A. Sakakibara, 2002: Large-scale parallel computing of cloud resolving storm simulator. *High Performance Computing*, H. P. Zima et al., Eds., Springer, 243–259.
- Ueno, K., K. Toyotsu, L. Bertolani, and G. Tartari, 2008: Stepwise onset of monsoon weather observed in the Nepal Himalaya. *Mon. Wea. Rev.*, **136**, 2507–2522, <https://doi.org/10.1175/2007MWR2298.1>.
- Vellore, R. K., and Coauthors, 2016: Monsoon–extratropical circulation interactions in Himalayan extreme rainfall. *Climate Dyn.*, **46**, 3517–3546, <https://doi.org/10.1007/s00382-015-2784-x>.
- Vishnu, S., W. R. Boos, P. A. Ullrich, and T. A. O’Brien, 2020a: Assessing historical variability of South Asian monsoon lows and depressions with an optimized tracking algorithm. *J. Geophys. Res. Atmos.*, **125**, e2020JD032977, <https://doi.org/10.1029/2020JD032977>.
- , —, —, and —, 2020b: Global track dataset of monsoon low pressure systems. Zenodo, accessed 19 October 2022, <https://doi.org/10.5281/zenodo.3890646>.